Chemical Engineering Science 137 (2015) 9–21

Contents lists available at ScienceDirect

Chemical Engineering Science

journal homepage: www.elsevier.com/locate/ces

On-line measurement of the real size and shape of crystals in stirred tank crystalliser using non-invasive stereo vision imaging

Rui Zhang [a,b], Cai Y. Ma [b], Jing J. Liu [a], Xue Z. Wang [a,b,*,1]

[a] School of Chemistry and Chemical Engineering, South China University of Technology, Guangzhou 510640, China
[b] Institute of Particle Science and Engineering, School of Chemical and Process Engineering, University of Leeds, Leeds LS2 9JT, UK

HIGHLIGHTS

- Crystal size and shape in a stirred crystalliser is measured using on-line 3D imaging.
- Off-line sample analysis shows on-line 3D imaging gives more accurate size than 2D.
- For needle like crystals, on-line 2D imaging typically under-estimates the length by 2/3.
- On-line 3D imaging and image analysis is also used to derive faced growth kinetics.

ARTICLE INFO

Article history:
Received 15 February 2015
Received in revised form
18 April 2015
Accepted 10 May 2015
Available online 14 June 2015

Keywords:
Stereo vision imaging
Image analysis
Crystallisation
3D reconstruction
Crystal size
L-glutamic acid

ABSTRACT

Non-invasive stereo vision imaging technique was applied to monitoring a cooling crystallisation process in a stirred tank for real-time characterisation of the size and shape of needle-like L-glutamic acid (L-GA) β polymorphic crystals grown from solution. The instrument consists of two cameras arranged in an optimum angle that take 2D images simultaneously and are synchronised with the lighting system. Each 2D image pair is processed and analysed and then used to reconstruct the 3D shape of the crystal. The needle shaped L-GA β form crystal length thus obtained is found to be in good agreement with the result obtained from off-line analysis of crystal samples, and is about three times larger than that estimated using 2D imaging technique. The result demonstrates the advantage of 3D imaging over 2D in measurement of crystal real size and shape.

1. Introduction

Crystallisation is an important operation widely used in industry to produce various particulate products such as pharmaceuticals and fine chemicals. The size and shape of crystals are key quality measures (Lovette et al., 2008) that should be measured on-line in real-time for the purpose of effective process optimisation and advanced control. The most widely studied process analytical technology (PAT) for on-line and real-time characterisation of crystal size and shape is focused-beam reflectance measurement (FBRM) that is based on laser light backscattering and measures particle cord length distribution (CLD). CLD can be used to estimate particle size distribution (Li et al., 2014; Mangold, 2012; Nere et al., 2006), but the error can be large if the particles deviate far from being spherical. Effort was also made to extract particle shape information from FBRM CLD measurements such as the imaginative work of (Ma et al., 2001; Yamamoto et al., 2002), but concern remains on the magnitude of error that is introduced in the conversion from CLD to crystal shape. Microscopy imaging is considered as probably the most promising technique for measuring particle shape since one can see the shape of the particles, as a result has attracted much attention in recent years. Calderon De Anda et al. (2005a, 2005b; De Anda, 2005), Wang et al. (2007) and Larsen et al. (Larsen and Rawlings, 2009; Larsen et al., 2006, 2007) used a GSK imaging system with non-invasive high-speed camera to record images and monitor the particle shape and size in a stirred batch crystalliser. Zhou et al. (2011, 2009) used image analysis to automatically extract the maximum possible information from in situ digital particle vision and measurement (PVM) images, which was employed to monitor particle shape and size distribution on-line.

Considering the fact that crystals in a stirred tank crystalliser undergo continuous rotation and motion, characterisation of the

* Correspondence to: School of Chemistry and Chemical Engineering, South China University of Technology, 381 Wushan Rd, Tianhe District, Guangzhou 510641, China. Tel./fax: +86 20 8711 4000.
E-mail addresses: xuezhongwang@scut.edu.cn, x.z.wang@leeds.ac.uk (X.Z. Wang).
[1] Tel.: +44 113 343 2427; fax: +44 113 343 2384.

http://dx.doi.org/10.1016/j.ces.2015.05.053
0009-2509/

size and shape of crystals based on 2D images can have big errors unless the crystals are close to sphere. Taking a needle-like crystal as an example for which we are mainly interested in its length. In a three dimensional Cartesian coordinate system, with origin O and axis lines X, Y and Z, a particle can randomly rotate, the probability of the needle-like perpendicular to the camera's optical axis is extremely small over all of the possible orientations. As a result, the 2D imaging technique cannot precisely measure the real size and shape; and the obtained size (i.e. length) is likely to be smaller than the real size.

Li et al. (2006) made probably the first attempt to obtain 3D crystal shape information based on on-line obtained images of crystallisation and presented a camera model for integrating both crystal morphological modelling and on-line shape measurement using 2D imaging. The 3D shape of crystals was predicted using the morphological modelling software HABIT (Clydesdale et al., 1996), then 3D shape rotation and a camera model were used for projecting 3D crystal on a 2D plate to generate a library of 2D images, finally matching between images in the library and the processed on-line images to identify the corresponding crystal with 3D sizes. Wang et al. proposed to use (Wang et al., 2008) two or more synchronised cameras to firstly obtain two or three 2D images of the same moving crystal from different angles and then reconstruct its 3D shape from the 2D images using a 3D reconstruction algorithm. Bujak and Bottlinger (2008) used the same principle to measure particle real 3D shape although their system is for measuring dry particles rather than particles in a slurry. Borchert et al. (2014) proposed an analogous estimation methodology to reconstruct the 3D crystal shape by comparing Fourier descriptors of the 2D crystal projection in pre-computed database with the Fourier descriptors of on-line measured 2D images. However, the size and shape information of crystals collected from a single direction is frequently incomplete, especially for shape estimation. Because of the small crystal thickness, the estimation for the crystal orientation is highly sensitive to the finite image resolution causing an inaccurate shape estimation (Borchert et al., 2014). An additional camera can help provide more accurate 3D shape information of the crystal, which will mitigate this problem and increase the accuracy of shape estimation. Therefore, for suspension crystallisation processes, stereoscopic imaging, i.e., photographing the same particle from multiple view directions, is a promising method to overcome the issue (Bujak and Bottlinger, 2008; Wang et al., 2008). A method of photographing from vertical directions using a single camera but two mirrors the same particles that flow through a cell was presented by Mazzotti and co-workers (Kempkes et al., 2010; Schorsch et al., 2012). The system was further improved based on their early work, i.e., replacing the mirrors with a second camera (Schorsch et al., 2014). Multidimensional particle size distribution is measured using the image acquisition setup. However, the particles are captured by two cameras when they flow through the cell rather than a stirred tank crystallizer. In addition, the concentration of solution is not measured on-line during the crystallisation processes, and kinetics of crystal growth is not presented.

Some other techniques were investigated to characterise 3D crystal shape in recent years such as tomography and optical sectioning. Tomography refers to imaging by sections or sectioning via the use of penetrating wave. Different images can be captured from each direction, and all collected images are used to reconstruct 3D crystal shape (Gonzalez and Woods, 2008; Midgley et al., 2007). Magnetite that ranges from decimetres to micrometres in size were identified and quantified to obtain crystal size distributions (CSDs) using X-ray tomography (Pamukcu and Gualda, 2010). Larson et al. (2002) developed a differential-aperture X-ray microscopy technique to make microstructure and stress/strain measurements with sub-micrometre point-to-point spatial resolution in three dimensions. Another approach for directly measuring 3D crystal shape, optical sectioning is popular in modern microscopy since it allows 3D reconstruction for a sample from images obtained at different focal planes. This technique is employed to analyse rock and mineral (Higgins, 2000; Jerram and Higgins, 2007; Jerram et al., 2009; Ketcham and Carlson, 2001), as it can obtain the inner information of crystal by splitting a 3D object tomultiple2D slices. A non-destructive technique with sectioning is the application of confocal optical microscope, which was reported in detail by Webb (1996). This microscope using optical sectioning technique is successfully applied to reconstruct the 3D shape of final crystal product (Castro et al., 2004; Conchello and Lichtman, 2005; Singh et al., 2012; Wilson, 2011). However, all the methods reviewed above in this paragraph require a sample preparation, which is time-consuming and costly. And these technologies therefore are generally used for off-line imaging of dry samples, not suitable for online measurement of the 3D shape of crystals in a suspension.

In summary, previous work on 3D imaging of the shape of growing crystals has used off-line and slow technique such as confocal microscopy, or been restricted to a small volume vial with no stirring, rather than stirred tank crystalliser. In addition, in previous work of on-line crystallisation imaging, solution concentration was not measured and no attempt was made to derive faceted crystal growth kinetics. Our previous work (Wang et al., 2007) measured solution concentration and derived growth rates but it was based on 2D imaging. In this study, an non-invasive on-line stereo vision imaging system, *Stereovision*^{NI}, was used to measure real crystal size and shape. In a previous study (Wang et al., 2008), a stereo vision imaging configuration involving two synchronised cameras was proposed. The work presented here builds upon the previous idea, focusing on estimating the real crystal size and validation in practical crystallisation process. The instrument, *Stereovision*^{NI} is a product of Pharmavision Limited and is based on fixing two cameras in an optimum angle and that are synchronised with the lighting system. It is non-invasive since it plays the cameras and lighting systems outside the glass walled crystalliser, avoiding some practical problems associated with directing contact with the slurry such as crystals sticking to the camera head. The collected 2D image series of needle-like β-polymorphic L-glutamic acid crystals were processed to reconstruct 3D crystal shape using the *Stereovision*^{NI} software also developed by Pharmavision Ltd. To verify the reliability of this method, the off-line imaging instrument, *Morphologi* G3 from Malvern Instruments Ltd., was applied to analyse the product size (here length) distribution. The results of 3D on-line imaging, 2D on-line imaging and off-line imaging are compared.

2. Experiments

2.1. Materials

L-glutamic acid (L-GA) selected for this study, $C_5H_9NO_4$, is one of the 20 known amino acids. The L-GA crystals are known to have two polymorphs (Davey et al., 1997; Kitamura and Ishizu, 2000), the prismatic α and the needle-like β forms. β-form L-GA crystals was crystallised in this research to demonstrate 3D reconstruction by the stereo imaging technique. Since it is of needle-like shape only one characteristic size, i.e. the length (L) is considered in this article. The solubility of β-form L-GA crystals can be estimated by Eq. (1) (Li et al., 2008), and the relative supersaturation can be calculated by Eq. (2).

$$C^* = 2.204 - 0.07322 * T + 0.00893 * T^2 - 0.000148183 * T^3$$

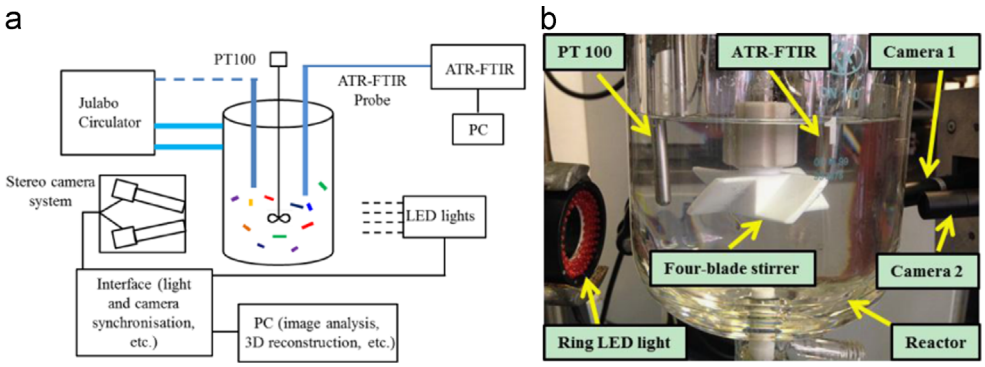

Fig. 1. Experimental set-up of the 1 L crystalliser equipped with the non-invasive stereo vision imaging system, (a) schematic, and (b) photo.

$$+0.00000134069*T^4 \quad (1)$$

$$S = C/C^* - 1 \quad (2)$$

where S is the relative supersaturation, T is the temperature in Celsius, C is the concentration and C^* is the solubility in g/L. The solid L-GA crystals were purchased from Van Waters and Rogers (VWR) International Ltd.

2.2. Experimental system setup

The 1 L rig used for the cooling crystallisation process is shown in Fig. 1. It was also used to prepare seeds using a cooling recrystallisation process. A Julabo FP50-HE thermostatic bath was employed to control temperature by oil circulation and a pitched four-blade stirrer rotating at 250 rpm was used to provide the reactor stirring. The temperature was measured using a platinum resistance thermometer (PT100). Solution concentration was monitored using attenuated total reflectance-Fourier transform infrared (ATR-FTIR) instrument, ReactIR 4000 from Mettler Toledo Ltd. PLS method (Ma and Wang, 2012a, 2012b; Wold et al., 2001) was used to develop the model. The model was built using calibration data include temperature from 10 to 80 °C, and concentration range 3–60 (g-LGA/L-water). The data was divided into two sets, the training dataset (47 spectra) for calibration model development and the test dataset (16 spectra) for model verification. In this work, the model was from the literatures (Ma and Wang, 2012a, 2012b). Because these instruments (1L crystallizer, the Julabo FP50-HE thermostatic bath, the stirrer and ATR-FTIR) and L-GA applied to the experiments are the same as the literature. Additionally, the operation conditions including temperature and concentration are also within the calibration data. Therefore, the model in the literature is suitable to this work.

The on-line imaging system employed in the experiments is depicted in Fig. 1. The system consists of two Basler avA1000-120 km cameras (camera 1 and camera 2) with identical specifications. The CCD camera fitted with Truesense Imaging sensor is employed for image acquisition with a maximum frequency of up to 120 images per second with a pixel resolution of 1024×1024 and a field of view with 2.82 mm × 2.82 mm dependent on calibrated lenses employed. In this study, it was set to capture 1 image per second. The 60 images in one minute were used for estimation of the mean length size of L-GA crystals for one specific time interval. A ring LED light source was used to provide illumination. The recorded images as video format were sent to a PC running *Stereovision*^{NI} software for acquisition, storage and management of the frames, and the measurement relative error of *Stereovision*^{NI} is less than 2%. It is worth noting that when applying the non-intrusive optical imaging system to a cylindrical reactor, the variation of refraction index of the medium in the reactor over temperature change, and the curved surface of the reactor may affect the quality of the captured images. However, the limited change of medium refraction against temperature variation (for example about 0.03% refraction index change of water for 1 °C temperature variation), the exactly same configuration, hence the same optic paths, of the two cameras and lenses, and the low curvature of the reactor surface over the small incident spot area indicate that their effects on the image quality and 3D reconstruction are very limited, which is indirectly supported by the measurement relative error of less than 2%.

In this work, seeds were added in the cooling crystallisation process to inhibit the secondary nucleation and the formation of tiny crystals. The β-form seed crystals were produced by slow cooling crystallisation and then washed, dried and sieved to provide the good initial size distribution for seeds. To carry out the experiment, a slurry was prepared with 13.5 g of L-GA in 500 mL of fresh distilled water. The solution was then heated quickly to 80 °C and held at the temperature for an hour with a constant agitation of 250 rpm. After 1 h, the ATR FTIR measured solution concentration was found to have kept constant at 13.5 g, which was consistent with the amount of added solids. In addition, it can be found from the captured images that the solution was clear without any solids at this moment. Therefore, it was reasonably believed that the solids were completely dissolved in the solution. The solution was then cooled down to 45 °C at a relatively fast rate of 1 °C/min. Two polymorphs of L-GA can be produced by controlling the cooling rate in batch crystallization (De Anda et al., 2005; Mougin et al., 2002). Only α-form crystals can be generated at cooling rate of 1 °C/min, while α-form transformed into β-form at cooling rate of 0.5 and 0.25 °C/min respectively (Calderon De Anda et al., 2005a, 2005b; De Anda, 2005), which indicates that a slow cooling rate should be used to obtain β-form L-GA crystals. To investigate needle-like β-form crystals during crystallisation, β-form L-GA seeds were added at the temperature 45 °C according to the Metastable Zone of L-GA (Borissova et al., 2008; Ma and Wang, 2012a), and a slow cooling rate of 0.05 °C/min was selected in the experiment. At the temperature of 45 °C, 0.27 g of seeds (2% of the solute (Chung et al., 1999; Kubota et al., 2001)) were added to the supersaturated solution, then the solution was cooled down at a cooling rate of 0.05 °C/min within 1 h. Observation and recording of process operation conditions (temperature, concentration and supersaturation) were conducted in real-time, as shown in Fig. 2. Obviously, the growth of β-form L-GA crystal happened with the decrease of the solute concentration during the cooling crystallisation. For estimation of crystal size, the temperature range used was from 45 to 42 °C and the corresponding relative supersaturation range was from 0.50 to 0.61.

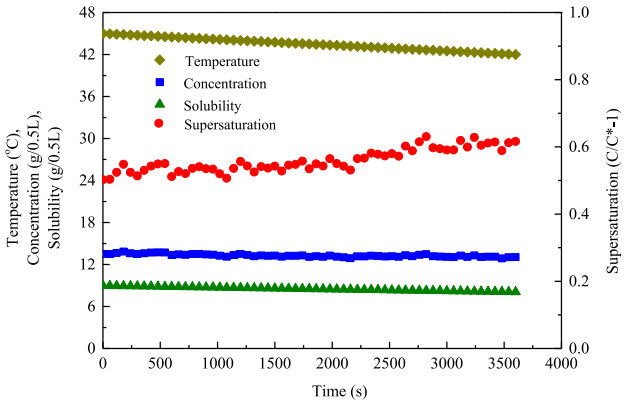

Fig. 2. Evolution of solution temperature (◆), concentration (▪),solubility (▲) and relative supersaturation (●) with time.

In order to further investigate the product shape and size information of final product, the solid products were quickly filtered with filter paper having pore size of 80–120 μm, then dried in vacuum oven for about 24 h at a constant temperature of 40 °C. The dried samples were measured with *Morphologi* G3. The filtration and vacuum drying processes used in this study can minimise their effects on the crystal size distribution. The 2D crystal shape and size distribution data were collected using the *Morphologi* G3 particle size and particle shape analyser from Malvern. The *Morphologi* G3 measures the size and shape of particles using the technique of static image analysis. Fully automation with integrated dry sample preparation makes it the ideal replacement for costly and time-consuming manual microscopy measurements. The measurement process can be described as follows: at first, the dry sample is prepared and uniformly dispersed on the measurement slide by a dry powder disperser. Next, the instrument captures images of individual particles by scanning the sample underneath the microscope optics, while keeping the particles in focus. Then, advanced graphing and data classification software provide a range of morphological analysis for each particle. Due to the effect of gravity, the needle-like L-GA β-form crystals intend to lie on the measurement plate. Therefore, it can be reasonably assumed that most particles dispersed on measurement plate are perpendicular to optic axis of the lens, therefore the *Morphologi* G3 can provide relative accurate size.

For on-line imaging of particles in suspension, image analysis is more complex and difficult compared to off-line imaging method. The main reason is the continuous motion of the slurries with constant agitation, which leads to the variation of distances between the camera lens and particles. As a result, some particles outside focal length of camera were quite blurred. Furthermore, the light effect and temporal changes of hydrodynamics within the reactor may result in varied brightness in the image background. In previous work a multistep multi-scale method was developed to extract objects from the image background in images from the GSK on-line microscopy system and off-line equipment (Calderon De Anda et al., 2005b). There are other methods developed in literature. The tool used in this study was developed by Pharmavision Ltd that has integrated various traditional image segmentation methods and newly published algorithms (Calderon De Anda et al., 2005b). For 3D reconstruction of particle size, the *Stereovision*^{NI} software employed in this work was developed in Pharmavision Ltd. The reconstruction approach mainly comprises five steps (Ma et al., 2014): multi-scale segmentation (Calderon De Anda et al., 2005b) of objects from the image background; region-filling and finding the centroid of objects; matching the particles from two cameras according to setting parameters in the programme; defining the vertices of matched crystals; and finally, calculating 3D coordinates of the crystals by triangulation method (Emanuele and Alessandro, 1998; Richard and Andrew, 2003). The 3D reconstruction procedure will be discussed below with the detailed algorithms for image segmentation (first step) being found in literature (Calderon De Anda et al., 2005b).

Using the multi-scale segmentation method (Calderon De Anda et al., 2005b), the crystals from each image of a stereo image pair are identified and numbered with the blurred crystals being automatically removed during the segmentation step and excluded in further processing steps. The reason to exclude blurred particles is because the size estimation is based on the assumption that the particle is at the focus. Inclusion of blurred particles will lead to error size estimation. By calculating the central coordinates of the identified crystals, and then comparing them in each image, the crystal pairs from the two images in an image pair can be identified. During this process, the crystals that are not paired will be automatically removed. The identified crystal pairs will then be processed for the purpose of corner/edge detection using methods in literature (Canny, 1986; Chris and Mike, 1988; Gonzalez and Woods, 2008) and feature-based matching algorithm (Gonzalez and Woods, 2008) to establish the feature (in this study, corner) correspondence. With the coordinates of corresponded corners, the reconstruction of the crystal can be achieved using the triangulation method that is described in literature (Emanuele and Alessandro, 1998; Richard and Andrew, 2003). With the current configuration of the imaging system, the stereo angle (α) between the two camera optic axes, the total distance (L) between a subject and camera including the lens working distance, lens length and camera flange focal distance, the magnification of the lenses (Δ) and the resolution (σ) have fixed values. The coordinates (X, Y, Z) of a corner in 3D space is a function of α, L, Δ, and the coordinates of the two 2D images (x_1, y_1, x_2, y_2), etc. and can be calculated by

$$\begin{bmatrix} X \\ Y \\ Z \end{bmatrix} = \begin{bmatrix} \frac{L}{2}+(x_1+x_2)\frac{\sigma}{\Delta} & 0 & 0 \\ 0 & y_1\frac{\sigma}{\Delta} & 0 \\ 0 & 0 & a+(x_2-x_1)\frac{\sigma}{\Delta} \end{bmatrix} \begin{bmatrix} \frac{\sin(\alpha/2)}{\sin\ \alpha} \\ 1 \\ \frac{\cos(\alpha/2)}{\cos\ \alpha} \end{bmatrix} \quad (3)$$

with α=54.5 mm, Δ=2, σ=0.00465 mm, α=22°. Using the reconstructed 3D coordinates, the crystal shape and size, and their distributions can be estimated.

3. Results and discussion

3.1. Off-line measurement of real crystal size

We will first introduce the off-line characterisation method that is used for validation of the on-line 3D imaging technique. In this study, *Morphologi* G3 was employed as the off-line characterisation method. It measures the morphological characteristics (size and shape) of dry crystals by dispersing the crystals on a plate. The particles dispersed on the measurement plate are automatically scanned by a camera in the measurement process. As the most stable position of a crystal in space should have the lowest free energy (Ma et al., 2012), the needle-like β-form L-GA crystals intend to position themselves in such a way that the largest {010} face is perpendicular to the vertical axis, i.e. the optical axis of the microscope. Hence size of the measured crystal is considered as real size, which will be used to compare with crystal size obtained by online measurement in the next section.

The size distributions of the added seeds and the dried final product of β-form L-GA crystals obtained at the end of the crystallisation process were analysed using *Morphologi* G3 software and are shown in Fig. 3. Fig. 3a and c show the shape and size distribution of crystal product. Fig. 3 also shows an overlapped

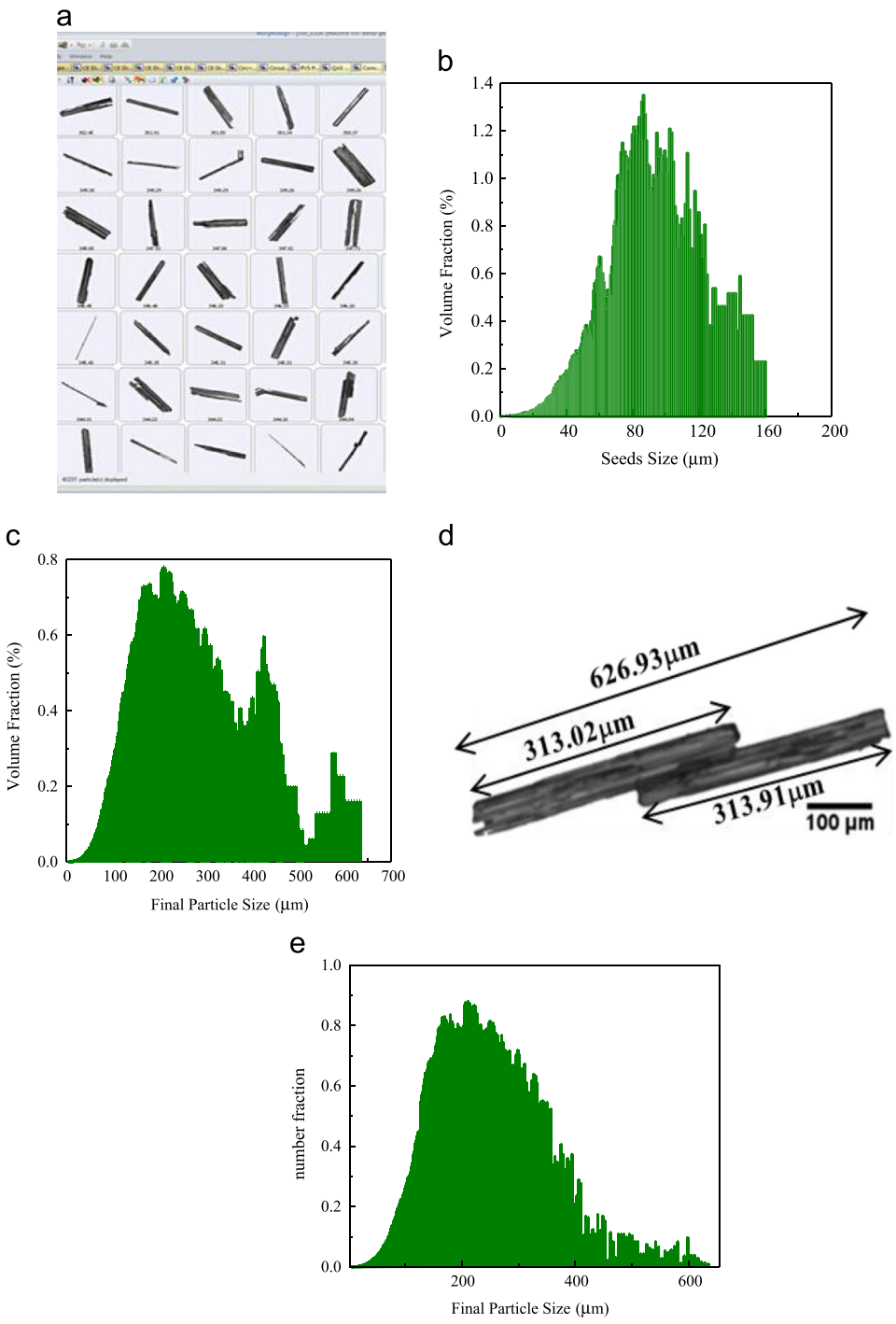

Fig. 3. Characterisation using the off-line instrument *Morphologi* G3 of (a) the shape of crystal product, (b) size (length) distribution of seeds (on volume basis) with a mean of 83.7 ± 2.1 μm, and (c) size (length) distribution of crystal product (on volume basis) with a mean of 207.7 ± 6.3 μm, (d) an example image of overlapped crystals captured using the off-line instrument *Morphologi* G3, (e) size (length) distribution of crystal product (on number basis). Data are representative of three separate experiments. Data represent the mean ± standard deviation (SD) of three independent experiments.

particle. Overlapped particles were treated as single ones in estimation of mean size distribution leading to measurement error. Fig. 3(d) shows such an example that two individual crystals of the length around 313.02 μm and 313.91 μm respectively gave a length of about 626.93 μm if the overlapped object is treated as a single particle. Therefore during dispersion, maximum power was set in order to minimise poor particle dispersion. This phenomenon might explain some large particle sizes observed in Fig. 3(c) in the range from 400 to 650 μm. In addition, ensemble particle sizing methods usually provide data on what is known as volume basis and number basis. On volume basis, the contribution each particle makes is proportional to its volume – large particles therefore dominate the distribution and sensitivity to small particles is reduced as their volume is so much smaller than the larger ones, while on number basis, the contribution each particle makes to the distribution is the same; a very small particle has exactly the same 'weighting' as a very large particle. In Fig. 3(c), the size distribution was based on volume weighting, hence bigger particle has larger effect on the distribution and bi-modal distribution appeared. While based on number weighting, as shown

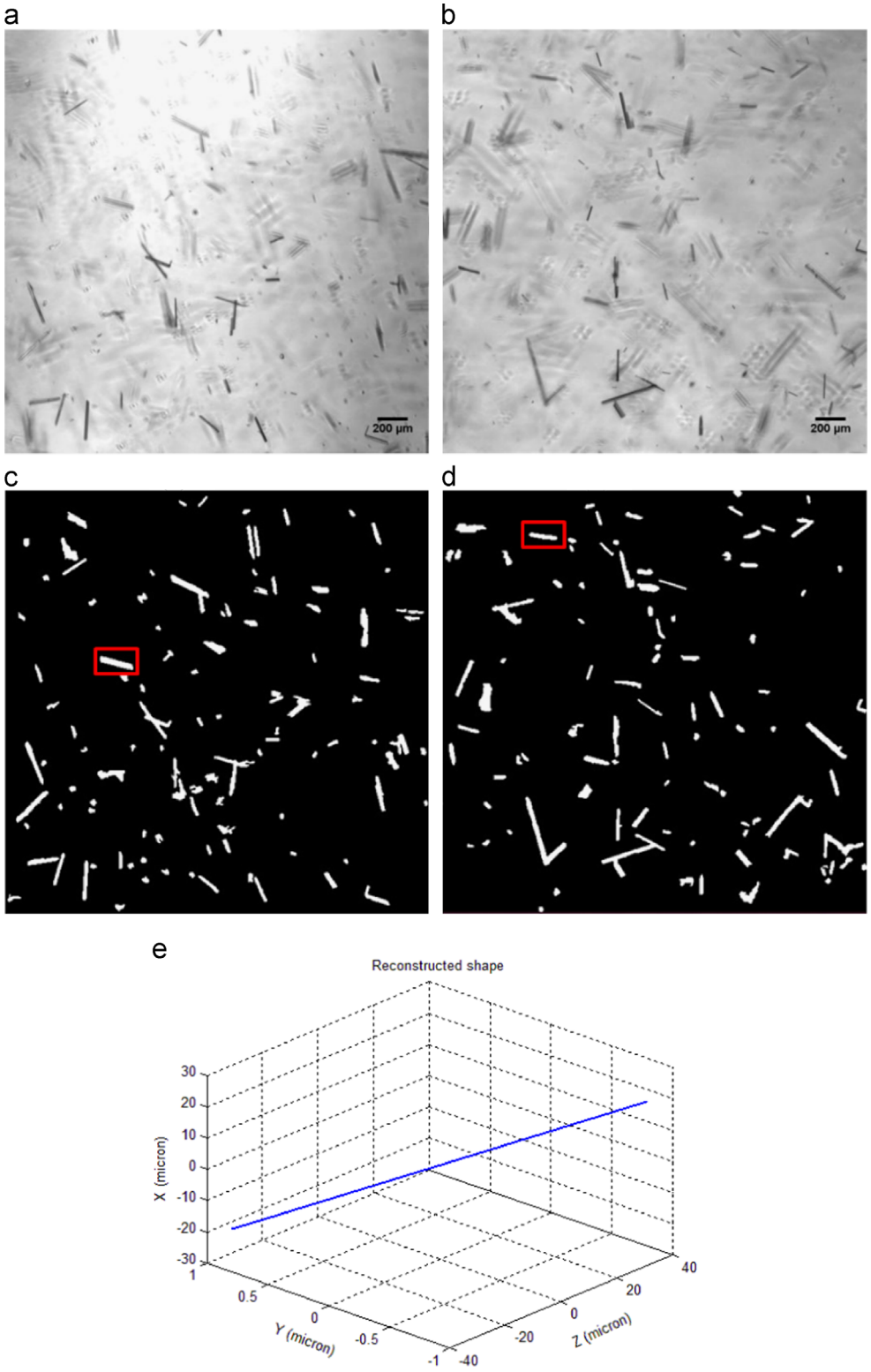

Fig. 4. On-line images from the stereo vision imaging system at $t=0$ s, (a) camera 1, (b) camera 2; a typical example of matched crystal images, (c) image from camera 1, (d) image from camera 2; (e) the matched 3D reconstruction crystal size, length=76.85 μm.

in Fig. 3(e), there is only mono distribution in the size distribution. Fig. 3(e) also shows the size distribution of the final product particles, indicating a mean of 205.1 ± 3.3 μm. It can be seen that the fraction of the size between 400 μm and 600 μm is lower than 0.1, which indicated that the effect of the large particles (i.e. particles possibly due to overlapping in dispersion) is small on the size distribution.

3.2. Online measurement of real crystal size

In this work, the particles in the crystalliser were simultaneously captured by two cameras from different orientations. The real size of crystals is the calculated after integrating imaging information obtained by the two cameras. The experiment lasted for 1 h, hence 3600 images were recorded during this period. To

reduce the time cost and estimate crystal size accurately, one image every two seconds was selected containing a total of 1800 high quality images to reconstruct 3D size of crystal.

Fig. 4–7 show images captured using on-line imaging system, processed images and the 3D reconstructed crystal size at four different time (t=0 s, 764 s, 2544 s and 3600 s).It can be observed that many crystals were captured by on-line imaging system each time, and some particles within focal length of cameras were clear, vice versa. In practice, the particles can be recorded only at a finite resolution on a CCD-chip. The size of particles depends on their pixel coordinates on the images. In order to precisely match the same particle on the images from two cameras, the difference between two pixel coordinates of the particle on the X and Y axis in two images have been calibrated in advance according to the

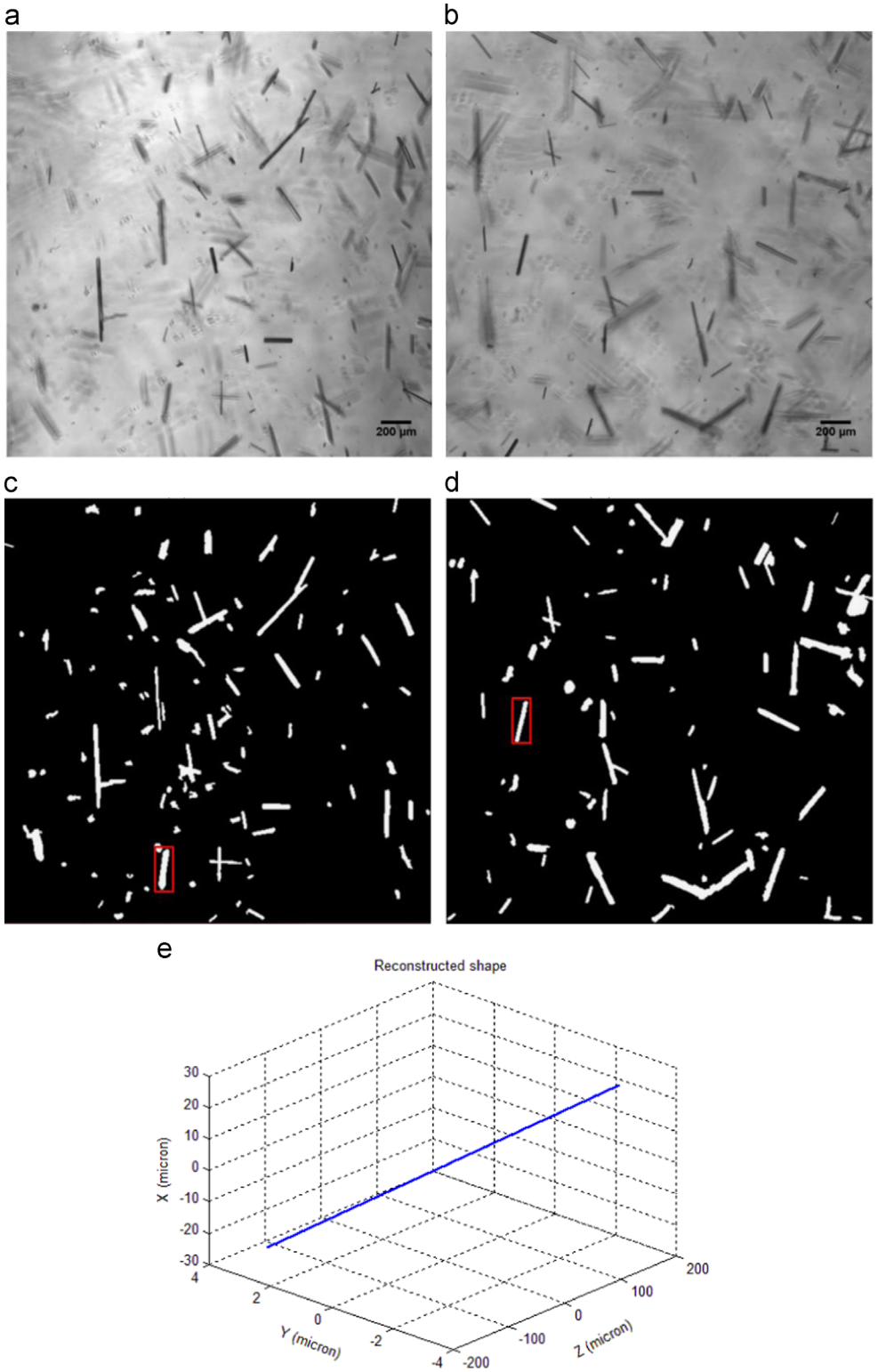

Fig. 5. On-line images from the stereo vision imaging system at t=764 s, (a) camera 1; (b) camera 2; a typical example of matched crystal images, (c) image from camera 1, (d) image from camera 2; (e) the matched 3D reconstruction crystal size, length=277.34 μm.

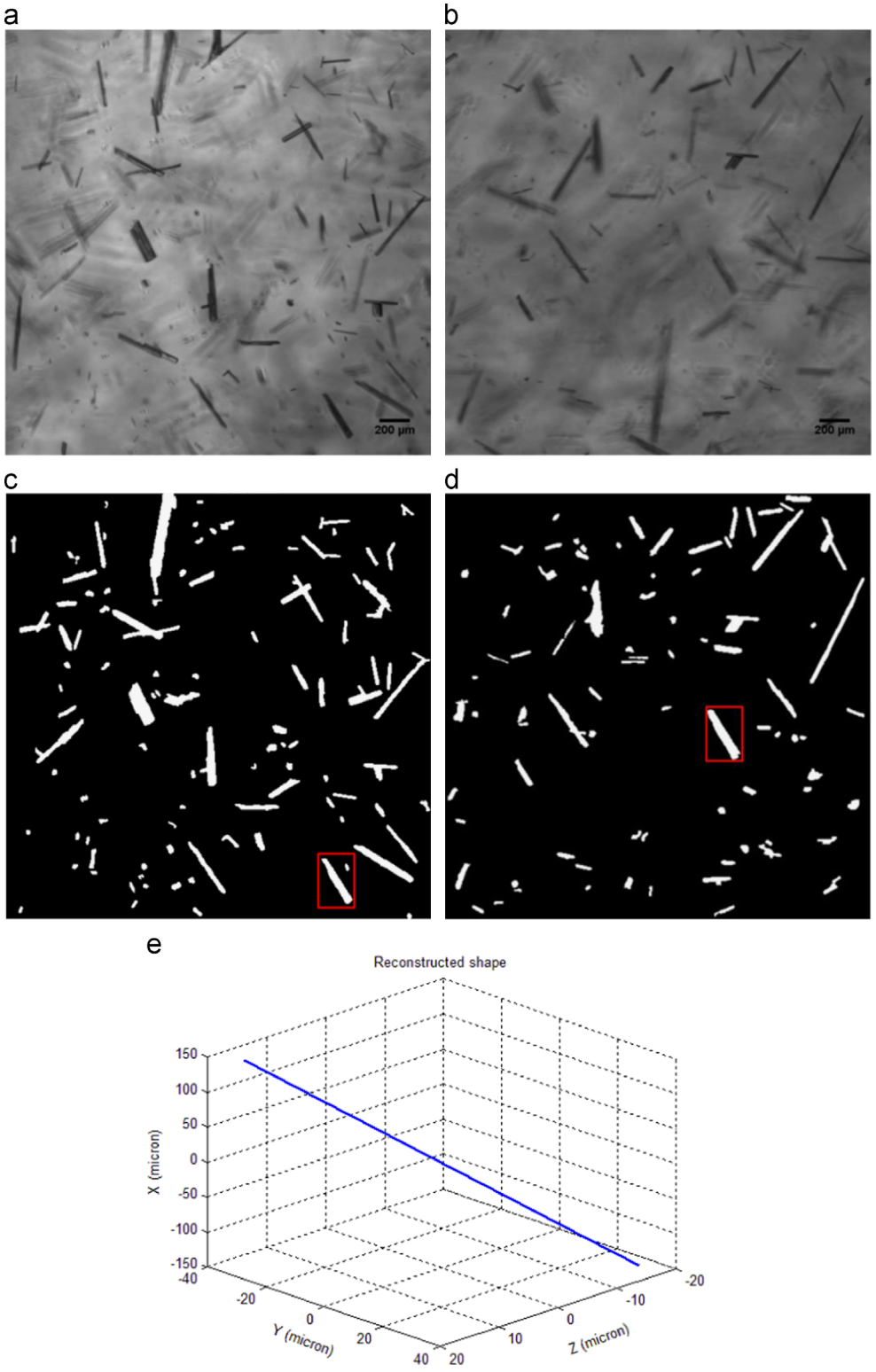

Fig. 6. On-line images from stereo vision imaging system at $t=2544$ s, (a) camera 1, (b) camera 2; a typical example of matched crystal images, (c) image from camera 1, (d) image from camera 2; (e) the matched 3D reconstruction crystal size, length=298.89 μm.

relative position of two cameras. *Stereovision*^{NI} software will automatically match the crystals in pictures captured by two cameras based on the calibration parameters (error and the difference of pixel coordinates). The number of crystals reconstructed successfully is uncertain each time, which depends on the contrast between particles and the background of images. Here we only present a few typical examples of crystals reconstructed to demonstrate this process. In Figs. 4e–7e, the crystal sizes obtained from 3D reconstruction are 76.85 μm, 277.34 μm, 298.89 μm and 311.80 μm at $t=0$ s, 764 s, 2544 s and 3600 s respectively, which indicates crystals grow gradually during the cooling crystallisation.

It is an apparent that it is impossible to capture the same crystals at different time intervals due to the continuous motion and rotation of the suspension in a reactor. Therefore, in order to

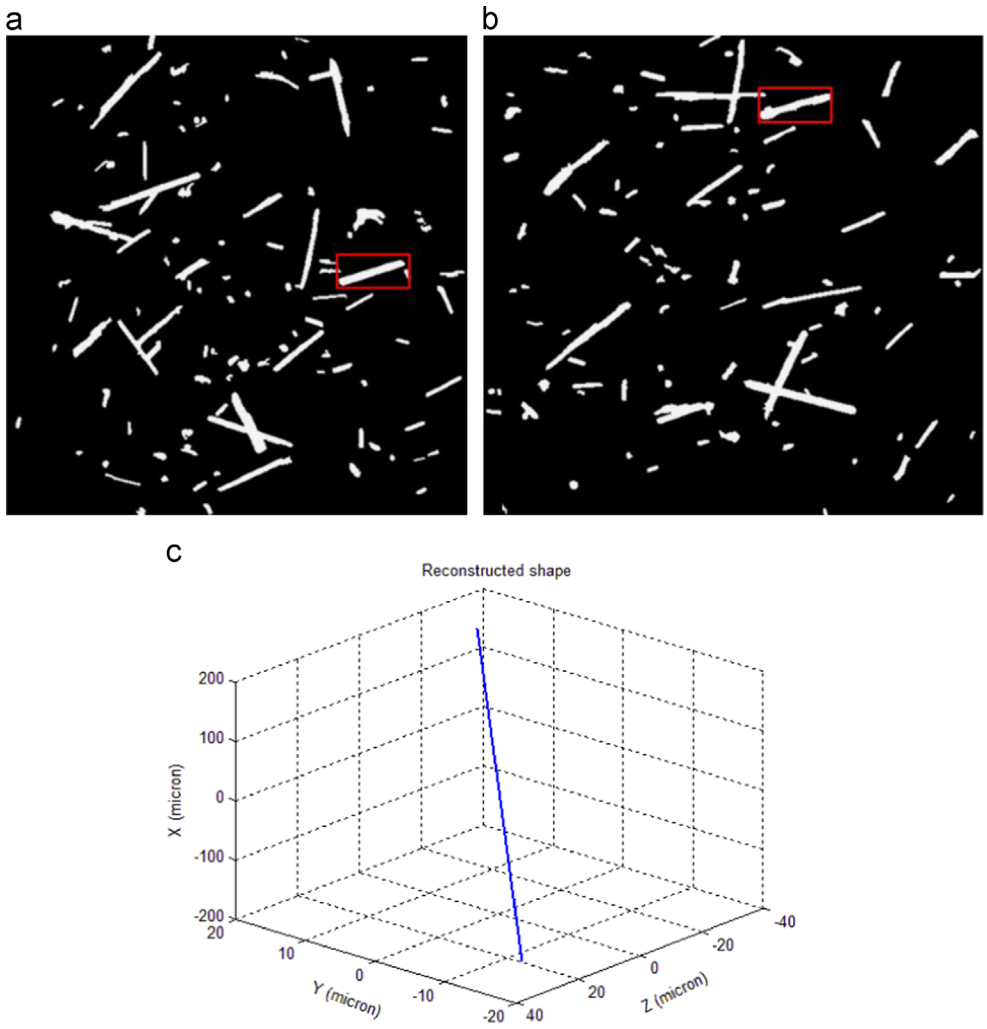

Fig. 7. An example of a matched crystal image at $t=3600$ s, from (a) camera 1, and (b) camera 2; and the 3D reconstruction of crystal size (length = 311.80 μm).

statistically estimate the variation of the crystal size with time, a moving time window approach was employed, the width of the time window is 20 s. Every time a new image is acquired, the earliest image in the window will be taken out to keep the window width at 20 s. All the particles in the current time window are analysed to give the size distribution information. The number of collected crystals (on the average) was around 25 at each time window. Fig. 8 displays the mean size distribution at different times based on analysed images from camera 1. As can be seen from Fig. 8, the mean size grew with time, and a linear function was used to curve-fit the data with R^2 being 0.90, the corresponding linear growth rate being 0.53×10^{-8} m/s. In addition, the size distribution at the 764th s, 2544th s and 3600th s are illustrated in Fig. 8a–c respectively. It needs to point out that the crystal size distribution at each time instant is calculated based on images collected in the last 60 s until the time constant. In other words the time window is 60 s. It can be observed that the size distributions exhibit narrow size distributions in Fig. 8a and b, which indicates that the sizes during these two periods are more uniformly distributed. The corresponding mean sizes are 37.21 μm and 49.11 μm, respectively. However, the size distribution in Fig. 8c is wider than that of Fig. 8a and b, which shows that there is a relatively sharp fluctuation at this period. The reasons leading to this phenomenon are still not clear since there is not sufficient information to explain it from these figures. However, some reasons might have caused the oscillation, such as breakage and agglomeration of crystals during the crystallisation processes. It is worth mentioning that this explanation is only an assumption rather than decisive. Nevertheless, we still report the data here as it was collected. It is also to note that there is the maximum value and the minimum value at the 3600th s, as shown in Fig. 8, which may be caused by the continuous motion of suspension. The crystals were easily broken by stirring blade with the size increase, which can result in the appearance of small crystals. On the other hand, the recorded much larger crystals on the 2D image may be emerged as a result of the overlapping crystals. The same method was used to analyse images from camera 2, as shown in Fig. 9. Obviously, they have the same trend for the mean size against time as Fig. 8. Correspondingly, the distributions were both narrow in the previous 20 s at 764 s and 2544 s (see Fig. 9a,b), while a wider size distribution was observed in Fig. 9c. Furthermore, the growth rate was 0.68×10^{-8} m/s using a linear function to curve-fit the relationship between the mean size and time with R^2 being 0.91 in Fig. 9. Fig. 10 shows the relationship between mean size and time after 3D reconstruction. The standard deviations of the size distributions are almost same as the results from camera 1 and camera 2 in the previous 60 s at 764 s, 2544 s and 3600 s, respectively.

Additionally, a linear function was also used to curve-fit them with R^2 being 0.90 in Fig. 10 as well as Figs. 8 and 9, hence the

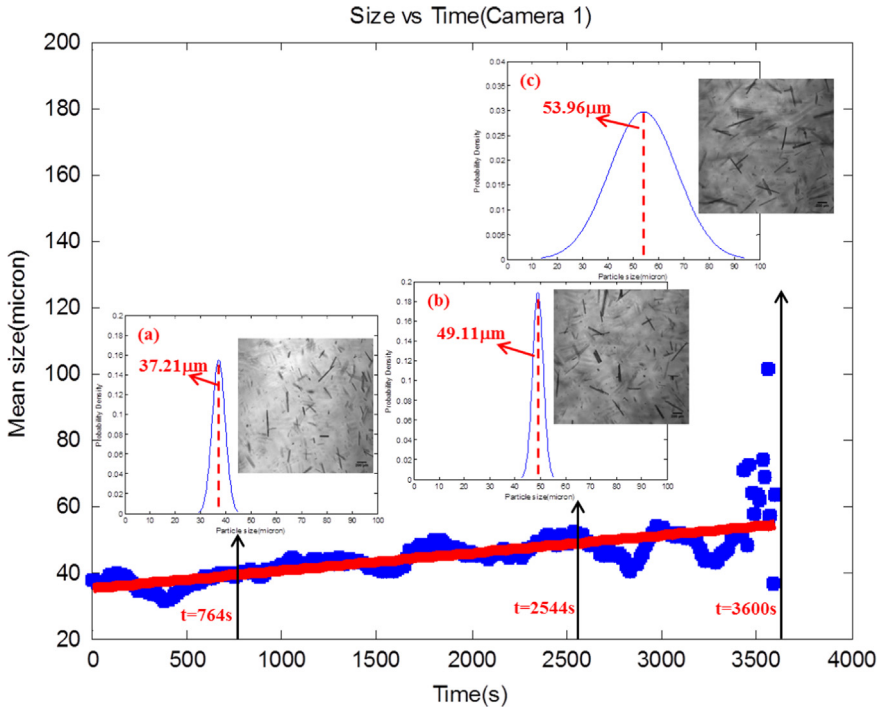

Fig. 8. Evolution of crystals size from camera 1, the mean size in time window of 20 s (•), the estimated mean size after the least-squares method fitting (−), growth rate $=0.53\times10^{-8}$ m/s, and the images from camera 1 at different time,(a) crystal size distribution during the previous 60 s at $t=764$ s, mean size$=37.21$ μm; (b) crystal size distribution during previous 60 s at $t=2544$ s, mean size$=49.11$ μm; (c) crystal size distribution during the previous 60 s at $t=3600$ s, mean size$=53.96$ μm.

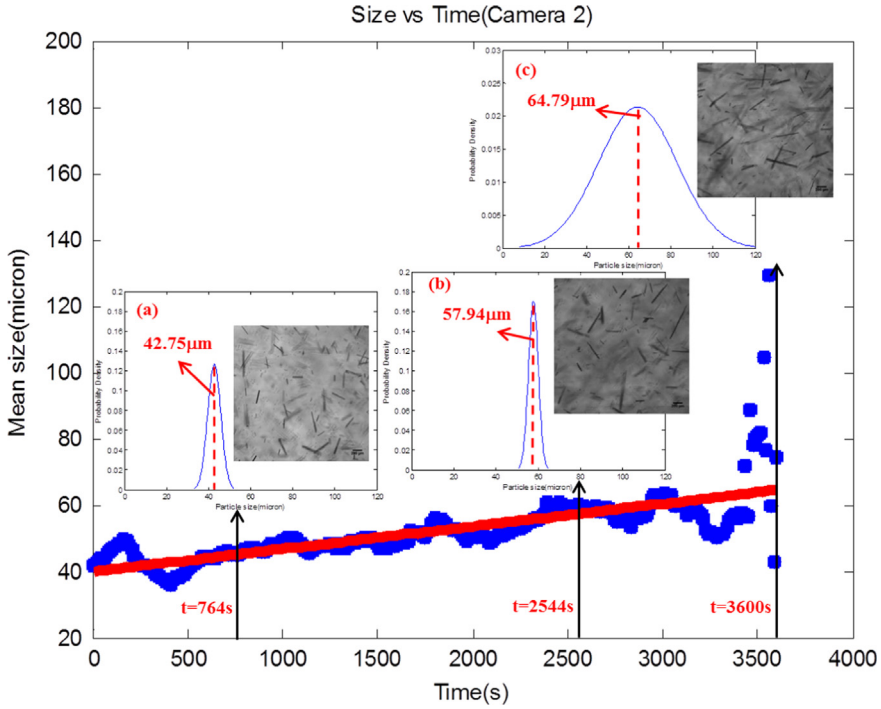

Fig. 9. Evolution of crystals size from camera 2, the mean size in time window of 20 s (•), the estimated mean size after the least-squares method fitting (−), growth rate $=0.68\times10^{-8}$ m/s, and the images from camera 2 at different time, (a) crystal size distribution during the previous 60 s at $t=764$ s, mean size$=42.75$ μm; (b) crystal size distribution during the previous 60 s at $t=2544$ s, mean size$=57.94$ μm; (c) crystal size distribution during the previous 60 s at $t=3600$ s, mean size$=64.79$ μm.

growth rate was 1.86×10^{-8} m/s after 3D reconstruction, which is much larger than the growth rate from either camera 1 or camera 2. It can be interesting to compare the results with the work in the literature (Kitamura and Ishizu, 2000; Ma and Wang, 2012b; Mougin et al., 2002; Wang et al., 2007). In this study, the change in crystal length was investigated, so the comparison is shown in Table 1 for the length direction only. Given the fact that these experiments were carried out in different operating conditions and using different measurement methods, the results can be regarded as having a good agreement. The growth rates in Figs. 8,

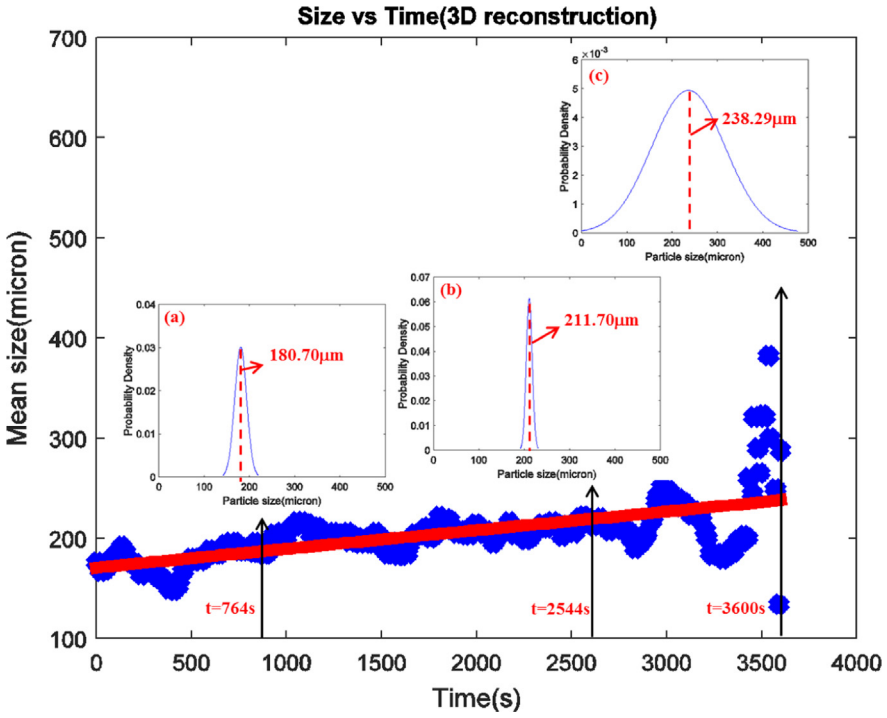

Fig. 10. Evolution of crystals size after 3D reconstruction, the mean size in time window of 20 s (•), the estimated mean size after the least-squares method fitting (–), growth rate = 1.86×10^{-8} m/s, (a) crystal size distribution during the previous 60 s at t = 764 s, mean size = 180.70 μm; (b) crystal size distribution during the previous 60 s at t = 2544 s, mean size = 211.70 μm; (c) crystal size distribution during the previous 60 s at t = 3600 s, mean size = 238.29 μm.

Table 1
Contrast of growth rate for μ-form L-GA in the length direction at supersaturation of 0.5.

References	Growth rate (m/s)	Crystallisation conditions	Instrument
Kitamura and Ishizu (2000)	1.3×10^{-8}	Isothermal crystallisation at 25 °C; single crystal growth in a flow cell	Microscope and video TV system
Mougin et al. (2002)	3.10×10^{-8}	Cooling crystallisation with a cooling rate of 0.1 °C/min; marine-type turbine (200 rpm); 3 L sample chamber; 2 wt% solution concentration	Ultrasizer (Malvern Instruments Ltd.)
Wang et al. (2007)	2.997×10^{-8}	Cooling crystallisation with a cooling rate of 0.1 °C/min; retreat curve impeller (300 rpm); 0.5 L glass jacketed batch reactor; 6.3 wt% solution concentration	On-line digital video microscopy system
Ma and Wang (2012b)	3.37×10^{-8}	Cooling crystallisation with a cooling rate of 0.1 °C/min; retreat curve impeller (250 rpm); 1 L glass jacketed batch reactor; 2.7 wt% solution concentration	PVS830 microscopy system and ATR-FTIR
This work	1.86×10^{-8}	Cooling crystallisation with a cooling rate of 0.05 °C/min; retreat curve impeller (250 rpm); 1 L glass jacketed batch reactor; 2.7 wt% solution concentration	Non-invasive Stereo Vision imaging system and ATR-FTIR

9 and 10 were all obtained using the least-squares method to fit the mean size and time. The linear regression may be not good because of the sharp fluctuation of the mean size at the last 100 s. If the data during this period is excluded from the results, it can be believed that the fitting results may be much better. However, in order to more realistically show this situation, these data are still retained in these figures.

From Figs. 8 to 10, it can be found that the estimated 3D crystal sizes are about three times larger than the calculated crystal sizes when only based on 2D images from a single camera, which corresponds to the difference of their growth rates. Actually, only taking into account camera 1 or camera 2 is equivalent to 2D on-line imaging measurement. Noting that the estimated particle sizes depend on their orientations in space for 2D measurement, and the obtained size can be much smaller than the real size in most cases. Therefore, if the crystal can be projected on two imaging plane, which may resolve the problem of the orientation dependence. In addition, it is interesting to find that the mean size sharply decreases at about the 3200th s and then rapidly rises again after 100 s, and becomes much larger at the time range from 3500 to 3600 s in Figs. 8 and 9. Similar findings can be found for the variation of the mean size in Fig. 10 after 3D reconstruction. This phenomenon may be caused by crystal breakage and agglomeration during the crystallisation process. The longer crystals are more likely to be broken by the stirring blade, which leads to mean size decrease. Furthermore, these broken crystals may be easier to overlap, which can result in the wider size distribution at the end. Overlapping crystals were found from images photographed by the on-line imaging system (for space consideration no figures will be given here). It is worth mentioning that this conclusion is not decisive, rather, it is only an assumption. Actually, if the time window calculating the mean size is set to be bigger, for example, 40 s or 1 min, the oscillation can be effectively reduced. However, we did not do that in order to objectively describe the case. As shown in Fig. 10, the mean size is 238.29 μm for the final product with the aid of 3D reconstruction method, which was found to be consistent with the size of 207.7 ± 6.3 μm obtained from the off-line measurement with *Morphologi* G3. According to the working principle of the *Morphologi* G3, the needle-like particles of β-form L-glutamic acid are perpendicular to the camera's optical axis in the measurement process. Therefore, the measured particle size using the instrument is considered as real size, which indicates

that the size of crystal measured by stereo vision imaging can be regarded as real size. The measurement method for 3D crystal size is more reasonable and reliable compared to on-line 2D imaging technique.

4. Conclusion

As anticipated the 3D on-line imaging system gives larger length for the needle like β form L-glutamic crystals than 2D imaging, qualitatively proving the need to replace 2D imaging using 3D. Quantitatively the 3D on-line measurement is validated by taking samples out of the reactor, letting the crystals lay down on a plate before analysing them using an instrument called *Morphologi* G3 that can analyse a population of particles. The crystal size measured by the 3D imaging system is in good agreement with that from the off-line system, whilst the calculated sizes based on 2D images are much smaller. Future work will investigate more complex shaped crystals using the on-line non-invasive stereo vision imaging technique to determinate crystal growth rates of individual facets and also apply in on-line monitoring and control of crystallisation processes.

Nomenclature

L-GA	L-glutamic acid
FBRM	focused-beam reflectance measurement
PVM	particle vision measurement
ATR-FTIR	attenuated total reflectance-Fourier transform infrared

Acknowledgements

Financial support from the China One Thousand Talent Scheme, the National Natural Science Foundation of China (NNSFC) under its Major Research Scheme of Meso-scale Mechanism and Control in Multi-phase Reaction Processes (project reference: 91434126), as well as Natural Science Foundation of Guangdong Province (project reference: reference: 2014A030313228, Scale-up study of protein crystallisation based on modelling and experiments) is acknowledged. The authors would like to thank Dr Wenjing Liu for helping with the setup of the experimental system. The authors would like to extend their thanks to Yu Jiao Liu and Ming Yue Wan of Pharmavision (Qingdao) Intelligent Technology Limited who provided the non-invasive on-line 3D imaging instrument *Stereovision*^{NI} the 3D reconstruction software as well as technical help. Thanks are also due to the Overseas Study Programme of Guangzhou Elite Project (GEP) in China for providing the first author a scholarship allowing him to carrying out visiting PhD research in the University of Leeds.

References

Borchert, C., Temmel, E., Eisenschmidt, H., Lorenz, H., Seidel-Morgenstern, A., Sundmacher, K., 2014. Image-based in situ identification of face specific crystal growth rates from crystal populations. Cryst. Growth Des. 14, 952–971.

Borissova, A., Khan, S., Mahmud, T., Roberts, K.J., Andrews, J., Dallin, P., Chen, Z.-P., Morris, J., 2008. In situ measurement of solution concentration during the batch cooling crystallisation of L-glutamic acid using ATR-FTIR spectroscopy coupled with chemometrics. Cryst. Growth Des. 9, 692–706.

Bujak, B., Bottlinger, M., 2008. Three-dimensional measurement of particle shape. Part. Part. Syst. Charact. 25, 293–297.

Calderon De Anda, J., Wang, X.Z., Lai, X., Roberts, K.J., 2005a. Classifying organic crystals via in-process image analysis and the use of monitoring charts to follow polymorphic and morphological changes. J. Process Control 15, 785–797.

Calderon De Anda, J., Wang, X.Z., Roberts, K.J., 2005b. Multi-scale segmentation image analysis for the in-process monitoring of particle shape with batch crystallisers. Chem. Eng. Sci. 60, 1053–1065.

Canny, J., 1986. A computational approach to edge detection. pattern analysis and machine intelligence. IEEE Trans. PAMI 8, 679–698.

Castro, J.M., Cashman, K.V., Manga, M., 2004. A technique for measuring 3D crystal-size distributions of prismatic microlites in obsidian. Am. Mineral. 88, 1230–1240.

Chris, H., Mike, S., 1988. A combined corner and edge detector. In: Proceedings of the 4th Alvey Vision Conference, pp. 147–151.

Chung, S.H., Ma, D.L., Braatz, R.D., 1999. Optimal seeding in batch crystallisation. Can. J. Chem. Eng. 77, 590–596.

Clydesdale, G., Roberts, K.J., Docherty, R., 1996. HABIT95 – a programme for predicting the morphology of molecular crystals as a function of the growth environment. J. Cryst. Growth 166, 78–83.

Conchello, J.A., Lichtman, J.W., 2005. Optical sectioning microscopy. Nat. Methods 2, 920–931.

Davey, R.J., Blagden, N., Potts, G.D., Docherty, R., 1997. Polymorphism in molecular crystals: stabilization of a metastable form by conformational mimicry. J. Am. Chem. Soc. 119, 1767–1772.

De Anda, J.C., Wang, X.Z., Lai, X., Roberts, K.J., Jennings, K.H., Wilkinson, M.J., Watson, D., Roberts, D., 2005. Real-time product morphology monitoring in crystallisation using imaging technique. AIChE J. 51, 1406–1414.

Emanuele, T., Alessandro, V., 1998. Introductory Techniques for 3-D Computer Vision. Prentice Hall.

Gonzalez, R.C., Woods, R.E., 2008. Digital Image Processing, 3rd ed. Prentice Hall.

Higgins, M.D., 2000. Measurement of crystal size distributions. Am. Mineral. 85, 1105–1116.

Jerram, D.A., Higgins, M.D., 2007. 3D analysis of rock textures: quantifying igneous microstructures. Elements 3, 239–245.

Jerram, D.A., Mock, A., Davis, G.R., Field, M., Brown, R.J., 2009. 3D crystal size distributions: a case study on quantifying olivine populations in kimberlites. Lithos 112 (Suppl. 1), S223–S235.

Kempkes, M., Vetter, T., Mazzotti, M., 2010. Measurement of 3D particle size distributions by stereoscopic imaging. Chem. Eng. Sci. 65, 1362–1373.

Ketcham, R.A., Carlson, W.D., 2001. Acquisition, optimization and interpretation of X-ray computed tomographic imagery: applications to the geosciences. Comput. Geosci. 27, 381–400.

Kitamura, M., Ishizu, T., 2000. Growth kinetics and morphological change of polymorphs of L-glutamic acid. J. Cryst. Growth 209, 138–145.

Kubota, N., Doki, N., Yokota, M., Sato, A., 2001. Seeding policy in batch cooling crystallisation. Powder Technol. 121, 31–38.

Larsen, P.A., Rawlings, J.B., 2009. The potential of current high-resolution imaging-based particle size distribution measurements for crystallisation monitoring. AIChE J. 55, 896–905.

Larsen, P.A., Rawlings, J.B., Ferrier, N.J., 2006. An algorithm for analyzing noisy, in situ images of high-aspect-ratio crystals to monitor particle size distribution. Chem. Eng. Sci. 61, 5236–5248.

Larsen, P.A., Rawlings, J.B., Ferrier, N.J., 2007. Model-based object recognition to measure crystal size and shape distributions from in situ video images. Chem. Eng. Sci. 62, 1430–1441.

Larson, B.C., Yang, W., Ice, G.E., Budai, J.D., Tischler, J.Z., 2002. Three-dimensional X-ray structural microscopy with submicrometre resolution. Nature 415, 887–890.

Li, H., Kawajiri, Y., Grover, M.A., Rousseau, R.W., 2014. Application of an empirical FBRM model to estimate crystal size distributions in batch crystallisation. Cryst. Growth Des. 14, 607–616.

Li, R.F., Thomson, G.B., White, G., Wang, X.Z., De Anda, J.C., Roberts, K.J., 2006. Integration of crystal morphology modeling and on-line shape measurement. AIChE J. 52, 2297–2305.

Li, R.F., Wang, X.Z., Abebe, S.B., 2008. Monitoring batch cooling crystallisation using NIR: development of calibration models using genetic algorithm and PLS. Part. Part. Syst. Charact. 25, 314–327.

Lovette, M.A., Browning, A.R., Griffin, D.W., Sizemore, J.P., Snyder, R.C., Doherty, M. F., 2008. Crystal shape engineering. Ind. Eng. Chem. Res. 47, 9812–9833.

Ma, C.Y., Liu, J., Liu, T., Wang, X., 2014. Development of a stereo imaging system for three-dimensional shape measurement of crystals. In: Proceedings of the 25th Chinese Process Control Conference, Dalian, China.

Ma, C.Y., Wan, J., Wang, X.Z., 2012. Faceted growth rate estimation of potash alum crystals grown from solution in a hot-stage reactor. Powder Technol. 227, 96–103.

Ma, C.Y., Wang, X.Z., 2012a. Closed-loop control of crystal shape in cooling crystallisation of L-glutamic acid. J. Process Control 22, 72–81.

Ma, C.Y., Wang, X.Z., 2012b. Model identification of crystal facet growth kinetics in morphological population balance modeling of L-glutamic acid crystallisation and experimental validation. Chem. Eng. Sci. 70, 22–30.

Ma, Z., Merkus, H.G., Scarlett, B., 2001. Extending laser diffraction for particle shape characterization: technical aspects and application. Powder Technol. 118, 180–187.

Mangold, M., 2012. Use of a Kalman filter to reconstruct particle size distributions from FBRM measurements. Chem. Eng. Sci. 70, 99–108.

Midgley, P.A., Ward, E.P.W., Hungria, A.B., Thomas, J.M., 2007. Nanotomography in the chemical, biological and materials sciences. Chem. Soc. Rev. 36, 1477–1494.

Mougin, P., Wilkinson, D., Roberts, K.J., 2002. In situ measurement of particle size during the crystallisation of L-glutamic acid under two polymorphic forms:

influence of crystal habit on ultrasonic attenuation measurements. Cryst. Growth Des. 2, 227–234.
Nere, N.K., Ramkrishna, D., Parker, B.E., Bell, W.V., Mohan, P., 2006. Transformation of the chord-length distributions to size distributions for nonspherical particles with orientation bias†. Ind. Eng. Chem. Res. 46, 3041–3047.
Pamukcu, A.S., Gualda, G.A.R., 2010. Quantitative 3D petrography using X-ray tomography 2: combining information at various resolutions. Geosphere 6, 775–781.
Richard, H., Andrew, Z., 2003. Multiple View Geometry in Computer Vision, 2 ed. Cambridge University Press.
Schorsch, S., Ochsenbein, D.R., Vetter, T., Morari, M., Mazzotti, M., 2014. High accuracy online measurement of multidimensional particle size distributions during crystallisation. Chem. Eng. Sci. 105, 155–168.
Schorsch, S., Vetter, T., Mazzotti, M., 2012. Measuring multidimensional particle size distributions during crystallisation. Chem. Eng. Sci. 77, 130–142.
Singh, M.R., Chakraborty, J., Nere, N., Tung, H.-H., Bordawekar, S., Ramkrishna, D., 2012. Image-analysis-based method for 3D crystal morphology measurement and polymorph identification using confocal microscopy. Cryst. Growth Des. 12, 3735–3748.
Wang, X.Z., Calderon De Anda, J., Roberts, K.J., 2007. Real-time measurement of the growth rates of individual crystal facets using imaging and image analysis: a feasibility study on needle-shaped crystals of L-glutamic acid. Chem. Eng. Res. Des. 85, 921–927.
Wang, X.Z., Roberts, K.J., Ma, C.Y., 2008. Crystal growth measurement using 2D and 3D imaging and the perspectives for shape control. Chem. Eng. Sci. 63, 1173–1184.
Webb, R.H., 1996. Confocal optical microscopy. Rep. Prog. Phys. 59, 427.
Wilson, T., 2011. Optical sectioning in fluorescence microscopy. J. Microsc. 242, 111–116.
Wold, S., Sjöström, M., Eriksson, L., 2001. PLS-regression: a basic tool of chemometrics. Chemom. Intell. Lab. Syst. 58, 109–130.
Yamamoto, H., Matsuyama, T., Wada, M., 2002. Shape distinction of particulate materials by laser diffraction pattern analysis. Powder Technol. 122, 205–211.
Zhou, Y., Lakshminarayanan, S., Srinivasan, R., 2011. Optimization of image processing parameters for large sets of in-process video microscopy images acquired from batch crystallisation processes: integration of uniform design and simplex search. Chemom. Intell. Lab. Syst. 107, 290–302.
Zhou, Y., Srinivasan, R., Lakshminarayanan, S., 2009. Critical evaluation of image processing approaches for real-time crystal size measurements. Comput. Chem. Eng. 33, 1022–1035.